

## Highlights

### **Resolving Primitive-Sharing Ambiguity in Long-Tailed Industrial Point Cloud Segmentation via Spatial Context Constraints**

Chao Yin, Qing Han, Zhiwei Hou, Yue Liu, Anjin Dai, Hongda Hu, Ji Yang, Wei Yao

- Identifies the “dual crisis”: 215:1 class imbalance compounded by high degree of geometric ambiguity where tail classes share cylindrical primitives with head classes.
- Introduces Boundary-CB and Density-CB spatial context constraints resolving primitive-sharing ambiguity through neighborhood prediction consistency.
- Presents interpretability analysis through intuitive metaphors and mathematical visualization of the proposed constraints.
- Achieves 55.74% mIoU on Industrial3D with 21.7% tail improvement (29.59% vs. 24.32% baseline) while preserving head accuracy (88.14%).
- Demonstrates dramatic gains on primitive-sharing components: reducer improves from 0% to 21.12% IoU and valve by 24.3% relative.

# Resolving Primitive-Sharing Ambiguity in Long-Tailed Industrial Point Cloud Segmentation via Spatial Context Constraints

Chao Yin<sup>a</sup>, Qing Han<sup>b</sup>, Zhiwei Hou<sup>c</sup>, Yue Liu<sup>a</sup>, Anjin Dai<sup>a</sup>, Hongda Hu<sup>a,c</sup>,  
Ji Yang<sup>a,d,\*</sup>, Wei Yao<sup>e,f,\*\*</sup>

<sup>a</sup>*Guangzhou Institute of Geography, Guangdong Academy of Sciences, Guangzhou, China*

<sup>b</sup>*School of Geography and Tourism, Hengyang Normal University, Hengyang, China*

<sup>c</sup>*Southern Marine Science and Engineering Guangdong Laboratory  
(Guangzhou), Guangzhou, China*

<sup>d</sup>*Guangzhou iMapCloud Intelligent Technology Co., Ltd., Guangzhou, China*

<sup>e</sup>*State Key Laboratory of Regional and Urban Ecology, Institute of Urban Environment,  
Chinese Academy of Sciences, Xiamen, China*

<sup>f</sup>*School of Engineering and Design, Technical University of Munich, Munich, Germany*

---

## Abstract

Industrial point cloud segmentation for Digital Twin construction faces a persistent challenge: safety-critical components such as reducers and valves are systematically misclassified. These failures stem from two compounding factors—such components are rare in training data, yet they share identical local geometry with dominant structures like pipes. This work identifies a “dual crisis” unique to industrial 3D data: extreme class imbalance (215:1 ratio) compounded by geometric ambiguity where most tail classes share cylindrical primitives with head classes. Existing frequency-based re-weighting methods address statistical imbalance but cannot resolve geometric ambiguity. We propose spatial context constraints that leverage neighborhood prediction consistency to disambiguate locally similar structures. Our approach extends the Class-Balanced (CB) Loss framework with two architecture-agnostic mechanisms: (1) **Boundary-CB**, an entropy-based constraint that emphasizes ambiguous boundaries, and (2) **Density-CB**, a density-based constraint that compensates for scan-dependent variations. Both integrate

---

\*Corresponding author. Email: yangji@gdas.ac.cn

\*\*Corresponding author. Email: wyao@iue.ac.cn

as plug-and-play modules without network modifications, requiring only loss function replacement.

On the Industrial3D dataset (610M points from water treatment facilities), our method achieves 55.74% mIoU with 21.7% relative improvement on tail-class performance (29.59% vs. 24.32% baseline) while preserving head-class accuracy (88.14%). Components with primitive-sharing ambiguity show dramatic gains: reducer improves from 0% to 21.12% IoU; valve improves by 24.3% relative. This resolves geometric ambiguity without the typical head-tail trade-off, enabling reliable identification of safety-critical components for automated knowledge extraction in Digital Twin applications. Code available at: <https://github.com/PointCloudYC/LongTail3D.git>.

*Keywords:* Spatial context constraints, Neighborhood entropy, Point cloud segmentation, Long-tailed learning, Digital twin, Industrial automation, Primitive-sharing ambiguity, 3D deep learning

---

## 1. Introduction

Digital Twin construction for industrial facilities requires accurate 3D point cloud semantic segmentation (PCSS) to extract functional component information [1, 2]. However, current methods systematically fail on safety-critical components like valves and reducers. These failures occur for two reasons: such components are rare in training data, and they share identical local geometry with dominant structures like pipes. We identify a unique challenge in industrial 3D data: a “dual crisis” where extreme class imbalance (215:1 ratio) compounds geometric ambiguity from primitive sharing between head and tail classes.

This dual crisis affects practical engineering applications. Digital Twin construction, facility management, and decision support systems rely on automated knowledge extraction [3, 4, 5]. While 3D acquisition technologies (LiDAR, photogrammetry) capture geometric data well, extracting semantic knowledge—identifying functional components like valves and pumps—remains difficult [6, 7, 8, 9]. Point Cloud Semantic Segmentation (PCSS) converts raw geometric data into structured knowledge for predictive maintenance and safety monitoring [10, 11, 12]. When PCSS fails on safety-critical components, the entire knowledge extraction pipeline breaks down.

Modern architectures perform well on benchmarks with moderate class imbalance, such as S3DIS [13] (7–50:1 ratios) and ScanNet [14] (20–30:1 ra-

tios). These include PointNet/PointNet++ [15, 16], transformers [17], and lightweight designs like RandLA-Net [18]. However, industrial scenes present a different challenge: extreme class imbalance ( $>200:1$ ) combined with geometric ambiguity where tail classes share primitives with head classes. Figure 1 compares S3DIS and Industrial3D datasets directly. Industrial environments show  $3.5\times$  greater statistical imbalance and significantly higher geometric ambiguity. Standard models fail on safety-critical components in these settings.

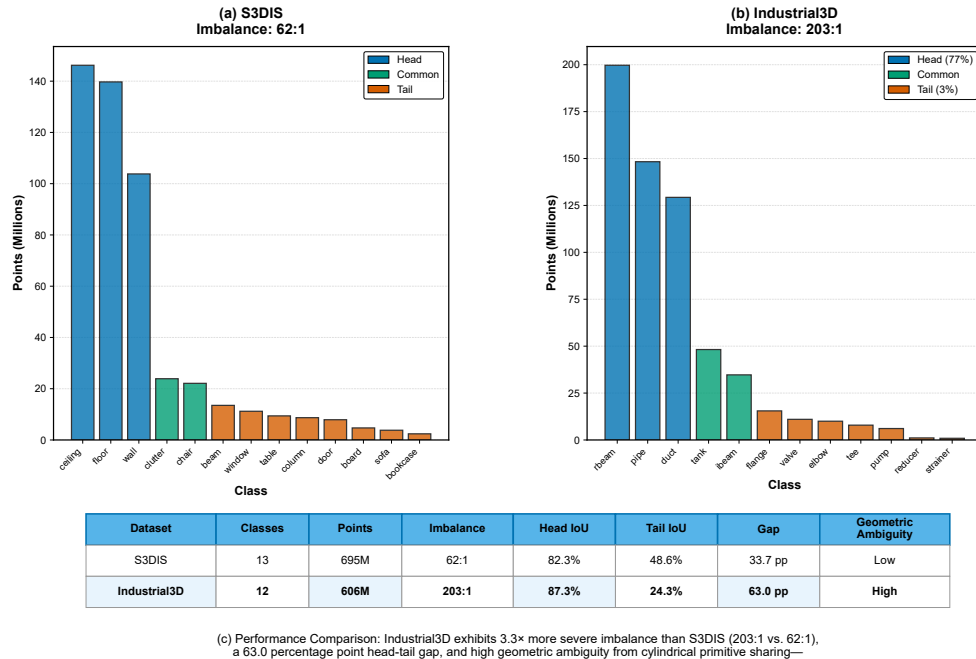


**Figure 1: Dataset Comparison Reveals Industrial3D’s Unique Dual Crisis. Panels (a-b):** Class distributions for S3DIS (indoor) and Industrial3D (water treatment facilities), showing head (blue), common (green), and tail (orange) classes sorted by frequency. **Panel (c):** Quantitative comparison table revealing Industrial3D’s dual crisis: (1) *Statistical severity*: 3.5 $\times$  more severe imbalance than S3DIS (215:1 vs. 62:1 ratio); (2) *Performance impact*: 63.0 percentage point head-tail gap (87.3% vs. 24.3% tail IoU) compared to 33.7 pp gap in S3DIS; (3) *Geometric ambiguity*: over 80% of tail classes share cylindrical primitives with Pipe, creating local indistinguishability. This combination of extreme statistical imbalance and systematic geometric ambiguity constitutes the dual crisis unique to industrial 3D segmentation and unaddressed by frequency-only methods. Abbreviation “rbeam” denotes rectangular beam.

Frequency-based re-weighting methods address extreme imbalance in 2D vision. Class-Balanced (CB) Loss [19] introduces the “effective number of samples” to formalize how additional samples provide diminishing marginal information. For a class  $c$  with  $n_c$  samples, the effective number is  $E_c = (1 - \beta^{n_c})/(1 - \beta)$ , where  $\beta$  controls information overlap. This formulation creates a ceiling effect: for large  $n_c$ ,  $E_c$  plateaus. This prevents the extreme gradients of naive inverse-frequency schemes while still boosting rare classes.

This 2D solution raises a question for 3D industrial data: **What factors beyond point count affect a class’s effective representation?** CB Loss treats all samples uniformly. This assumption fails when geometrically distinct objects (e.g., a Pipe vs. a Reducer) share identical local primitives (cylinders). Our analysis of the Industrial3D dataset reveals a structural pattern: head classes (beams, pipes; 77% of points) are predominantly long, continuous structures, whereas tail classes (3% of points) exhibit geometric heterogeneity. Tail classes split into two categories: *primitive-similarity* classes (e.g., elbows, reducers) that are locally indistinguishable from head-class pipes, and *composite-tail* classes (e.g., pumps, valves) whose individual components share geometry with head-class primitives.

To resolve this geometric ambiguity, we introduce **spatial context constraints** that use neighborhood prediction consistency to disambiguate locally similar structures. We formalize two complementary constraints extending the Class-Balanced (CB) framework: the **Boundary-CB constraint** adaptively emphasizes ambiguous boundaries by measuring neighborhood entropy, while the **Density-CB constraint** normalizes for scan-dependent density variations. Both constraints are architecture-agnostic and integrate into any point cloud pipeline without network modifications.

Our contributions are:

- **Problem formalization:** We formally characterize the “dual crisis” in industrial 3D point clouds—extreme statistical imbalance (215:1) compounded by geometric ambiguity where most of tail classes share primitives with head classes—and identify structural heterogeneity among tail classes (composite-tail vs. primitive-similarity).
- **Spatial context constraints:** We introduce Boundary-CB, which leverages neighborhood prediction consistency to resolve ambiguity from shared primitives, and Density-CB, which compensates for scan-dependent density variations, establishing geometry-aware long-tailed 3D learning.

- **Interpretability analysis:** Deep learning models are often criticized as black boxes that obscure their decision-making processes. We provide comprehensive interpretability through two complementary visualizations—intuitive metaphors (resource allocation, neighborhood consensus) and rigorous mathematical foundations—making the proposed constraints transparent and accessible to both researchers and practitioners.
- **Architecture-agnostic integration:** Our constraints function as plug-and-play modules compatible with any point cloud network without architectural modifications, enabling deployment in existing industrial pipelines.
- **Empirical validation:** On Industrial3D, Boundary-CB achieves 55.74% mIoU and 29.59% tail-class mIoU (+21.7% relative), demonstrating robustness on safety-critical components while preserving head-class accuracy—avoiding the typical head-tail trade-off.

This paper is organized as follows: section 2 reviews related work, section 3 details our proposed spatial context constraints, section 4 presents experimental validation, section 5 discusses implications for engineering informatics, and section 6 concludes.

## 2. Related Work

We review point cloud semantic segmentation and long-tailed learning methods to explain why existing approaches fail to address geometric ambiguity from primitive sharing in industrial data.

### 2.1. Fully Supervised Point Cloud Semantic Segmentation

Fully supervised methods learn from completely annotated data and dominate 3D semantic segmentation. These approaches fall into three categories: point-based, projection-based, or voxel-based [2]. Point-based networks operate directly on raw point clouds and have become the standard due to their architectural simplicity, efficiency, and ability to preserve geometric fidelity.

PointNet [15] pioneered permutation-invariant architectures for point sets. PointNet++ [16] introduced hierarchical feature learning to capture multi-scale local geometry, a concept that underpins most modern convolutional

neural network (CNN) architectures. Subsequent work produced more powerful local aggregation operators: RandLA-Net [18] uses random sampling and attention mechanisms for efficiency, KPConv [20] employs specialized kernel-based convolutions, and ResPointNet++ [7] integrates residual connections for complex industrial scenes. These methods work well on balanced benchmarks but degrade under the severe class imbalance of real-world industrial datasets.

Recent work has improved accuracy and efficiency: sparse voxel backbones using submanifold sparse convolutions [21], transformer-based designs such as Point Transformer v3 [17], unified segmentation frameworks like OneFormer3D [22], boundary-focused feature modeling (BFANet) [23], and analyses of local aggregation operators [24]. Large-scale annotation tools like ARKit LabelMaker [25] also expand dataset scale and supervision breadth. However, these advances primarily enhance representation capacity. They do not explicitly resolve long-tailed statistical bias or geometric ambiguity from primitive sharing in industrial data.

## 2.2. Deep Long-Tailed Learning

Long-tailed learning addresses training on datasets with severe class imbalance, where a few “head” classes dominate the distribution and numerous “tail” classes are under-represented [26]. Core strategies include re-sampling, data augmentation, and loss re-weighting [27, 28, 29, 19].

**Re-weighting vs. re-sampling.** In 2D vision, re-sampling (over-/under-sampling) can reduce bias but often overfits minority samples or discards informative majority examples. For point clouds, these problems get worse: point- or patch-level over-sampling distorts density statistics and breaks geometric continuity; under-sampling disrupts the geometric continuity required by kNN/ball-query operators. We therefore prefer loss re-weighting, which preserves native geometry while correcting gradient contributions.

Class-Balanced (CB) Loss [19] formalizes re-weighting via the “effective number of samples,” stabilizing training compared to naive inverse frequency scaling or smooth variants like inverse square root scaling [30, 31, 32]. Focal Loss [33] complements CB by down-weighting easy instances at the instance level. Their combination (CB+Focal) forms our strong frequency-based baseline.

**Augmentation.** MixUp/CutMix-style augmentation [28, 29] and standard 3D transforms (rotation, scaling, jitter) improve generalization but do

not directly correct class imbalance. They complement re-weighting approaches. However, frequency-only methods treat class members uniformly and ignore geometric factors—a limitation that becomes critical in 3D industrial data due to shared primitives between classes.

### 2.3. Long-Tailed Learning in 3D Point Clouds

Long-tailed learning for 3D point clouds is an emerging research area. Challenges exceed those in 2D due to unstructured representation, variable density, and occlusion—particularly pronounced in industrial environments with severe class imbalance ( $>200:1$ ), complex structures, and rare but critical components (e.g., pumps, valves).

**Recent 3D approaches.** Contemporary methods mitigate imbalance through sampling and optimization designs: two-stage/target-guided strategies for rare classes [34, 35], adaptive weight constraints with class-aware sampling [36], class-imbalanced semi-supervised schemes with decoupled optimization [37], and target-aware attentional networks for rare class segmentation [38]. These techniques primarily adjust data distribution or training objectives under label scarcity. They generally do not explicitly model geometric ambiguity and are complementary to our geometry-aware re-weighting.

**The Geometric Dimension of Imbalance.** Beyond statistical frequency, 3D point clouds introduce geometric ambiguity from systematic primitive-sharing between classes. Our analysis reveals a structural pattern: head classes (beams, pipes, ducts) have long-shaped, continuous geometry, whereas tail classes split into two categories. First, *composite-tail* classes (pumps, valves) are complex assemblies whose components share primitives with head classes, creating confusion at part boundaries. Second, *primitive-similarity tail* classes (elbows, tees, reducers) are simple objects locally indistinguishable from head-class pipes. This creates challenges that frequency-based methods cannot address:

1. **Compositional Ambiguity:** Composite-tail objects have boundary regions where local geometry matches head-class geometry, creating confusion at multi-part interfaces.
2. **Intrinsic Similarity:** Primitive-similarity tail objects (e.g., cylindrical elbows) share fundamental geometric primitives with head-class pipes. Local features are insufficient for discrimination, requiring global context.

**Limitations of Existing Approaches.** Recent 3D long-tailed learning methods [39, 40, 34, 35, 36, 37] and modern point cloud architectures [15, 20, 41, 42] typically adapt 2D frequency-based techniques without accounting for geometric factors. This addresses the *symptom* (statistical imbalance) but overlooks the *root cause* of misclassification in 3D data—geometric ambiguity from shared primitives. Our work explicitly leverages **spatial context constraints** to resolve this geometric ambiguity. We introduce constraints that measure neighborhood prediction consistency to identify and emphasize ambiguous boundaries, addressing both compositional and primitive-similarity ambiguity. Boundary-sensitive segmentation [23] and unified 3D frameworks [22] improve representations but do not mitigate frequency-driven bias that overwhelms tail classes. Our spatial context constraints are orthogonal and complementary to such architectural advances.

#### 2.4. Industrial Point Cloud Analysis

Industrial point cloud segmentation presents unique challenges. Our cross-dataset analysis of six benchmarks (see Supplementary Material) shows that industrial scenes combine extreme statistical imbalance with severe geometric ambiguity. Indoor scenes benefit from RGB texture and diverse geometries (S3DIS [13]: 15% geometric ambiguity; ScanNet [14]: 19%). Outdoor urban scenes have clear spatial separation (Semantic3D [43]: 20–25% geometric ambiguity). Industrial facilities exhibit systematic primitive-sharing. In Industrial3D, 86% of tail classes share cylindrical geometry with dominant head classes, creating local indistinguishability. This geometric homogeneity, combined with a 215:1 imbalance ratio, constitutes a dual crisis that is  $\sim 3.5 \times$  more severe statistically and  $4\text{--}5 \times$  worse geometrically than common benchmarks. Complementary work in AEC/MEP scenarios—vision-assisted BIM reconstruction [12], hierarchical segmentation with vision-language reasoning [44], robot-assisted mobile scanning [45], BIM-to-scan domain adaptation [46], label-efficient training [47, 48, 49], and cross-modal 2D–3D fusion [50] or BIM-generated synthetic supervision [9]—primarily reduces annotation cost or domain gaps. These approaches do not directly correct the long-tailed statistical and geometric imbalance that we target.

Even fine-grained taxonomies like ScanNet200 [51] (200 classes, 145:1 imbalance) exhibit only 32% geometric ambiguity and benefit from RGB texture unavailable in industrial data. Industrial applications require reliable segmentation of critical components for digital twins [47, 52], predictive

maintenance, and safety. Misclassifying a valve as a pipe can lead to incorrect flow analysis, faulty maintenance, or safety hazards. Existing long-tailed methods, developed for less imbalanced datasets, fail to address the geometric ambiguity inherent in industrial systems where head-class structures (pipes, beams) dominate both statistically (77% of data) and geometrically (through shared primitives). Our work targets this dual crisis by introducing **spatial context constraints** that leverage neighborhood prediction consistency to resolve geometric ambiguity.

### 3. Methodology

This section presents our spatial context constraints for resolving geometric ambiguity in long-tailed industrial point clouds. We propose two architecture-agnostic mechanisms that extend the Class-Balanced framework by incorporating spatial context: the **Boundary-CB** constraint for resolving geometric ambiguity through neighborhood entropy, and **Density-CB** for normalizing scan-dependent density variations. Figure 2 illustrates how these spatial context constraints integrate into standard point cloud segmentation pipelines as plug-and-play modules without requiring backbone modifications. We first formalize the dual crisis problem (§3.1), review the Class-Balanced (CB) Loss baseline (§3.2), then introduce our two spatial context constraints: **Density-CB** (§3.3) and **Boundary-CB** (§3.4). Finally, we specify evaluation metrics (§3.5).

#### 3.1. Problem Formulation: The Dual Crisis

Consider a training dataset  $\mathcal{D} = \{(P_i, Y_i)\}_{i=1}^{N_{\text{scene}}}$  of  $N_{\text{scene}}$  point cloud scenes. Each scene  $P_i = \{p_1^{(i)}, \dots, p_{M_i}^{(i)}\}$  contains  $M_i$  points, where  $p_j^{(i)} \in \mathbb{R}^3$  denotes the 3D coordinates of the  $j$ -th point in scene  $i$ . The corresponding labels are  $Y_i = \{y_1^{(i)}, \dots, y_{M_i}^{(i)}\}$ , where  $y_j^{(i)} \in \{1, \dots, C\}$  is the semantic class of point  $j$  from  $C$  total classes. For notational simplicity, we flatten all points across scenes into a single set of  $N = \sum_{i=1}^{N_{\text{scene}}} M_i$  points,  $\{p_1, \dots, p_N\}$ , with labels  $\{y_1, \dots, y_N\}$ .

In industrial scenes, the class frequency distribution is long-tailed. Let  $n_c = |\{i : y_i = c\}|$  be the number of points in class  $c$ . Since  $n_c$  varies by orders of magnitude, standard training is dominated by head classes, leading to poor generalization on rare but critical tail classes.

Beyond statistical imbalance, 3D point clouds introduce **geometric ambiguity**: systematic confusion between semantically distinct classes that

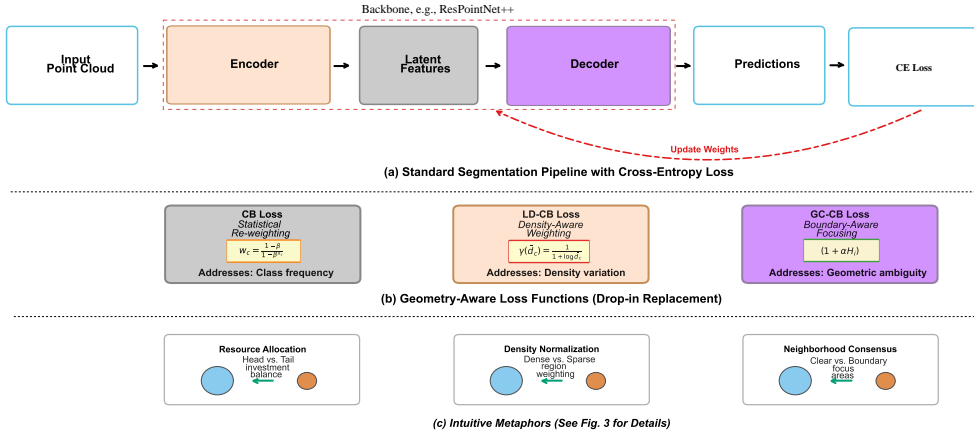


Figure 2: **Spatial Context Constraints Framework for Resolving Primitive-Sharing Ambiguity.** **Top (Pipeline):** Our architecture-agnostic framework augments standard point cloud segmentation pipelines (encoder-decoder backbone networks like ResPointNet++ or RandLA-Net) with spatial context constraints. The input 3D point cloud undergoes hierarchical feature extraction and upsampling to produce per-point predictions. Our constraints integrate as plug-and-play modules by replacing the standard cross-entropy loss  $\ell_{CE}$ , requiring no backbone modifications—critical for immediate industrial deployment. **Bottom (Three Constraints):** Three complementary mechanisms address orthogonal factors of the dual crisis: (1) **Class-Balanced (CB) Constraint** (Eq. 3): applies frequency-based re-weighting via effective number  $E_c = (1 - \beta^{n_c}) / (1 - \beta)$  computing weights  $w_c = (1 - \beta) / (1 - \beta^{n_c})$  (Eq. 2), correcting statistical class imbalance while preventing extreme re-weighting through ceiling effect; (2) **Density-CB** (Eq. 6): extends CB with density modulator  $\gamma(\bar{d}_c) = 1 / (1 + \log \bar{d}_c)$  (Eq. 7) from average local density  $\bar{d}_c$  within radius  $r$  (Eq. 5), compensating for scan-dependent spatial sparsity where dense regions (near scanner) are down-weighted and sparse regions (far from scanner) up-weighted; (3) **Boundary-CB** (Eq. 10): extends CB with entropy modulation  $(1 + \alpha H_i)$ , where neighborhood entropy  $H_i = -\sum_c \hat{p}_c^{(i)} \log \hat{p}_c^{(i)}$  (Eq. 9) quantifies prediction inconsistency across  $k$ -nearest neighbors  $\mathcal{N}_k(i)$ , **resolving geometric ambiguity from primitive sharing** by adaptively emphasizing ambiguous boundaries where tail classes (reducer, valve) share local geometry with head classes (pipe). Each constraint independently targets one crisis factor; Boundary-CB is recommended for industrial scenarios with severe geometric ambiguity.

share local geometric primitives. Unlike 2D images, where object categories typically have distinguishable local features, many objects in 3D industrial scenes are composed of identical geometric primitives, differing only in global structure or context.

Our analysis of the Industrial3D dataset shows a critical **structural prior**. Head classes (`RectangularBeam`, `Pipe`, `Duct`), comprising 77% of the dataset, are uniformly long-shaped, continuous structures. In contrast, tail classes (3% of points) display geometric heterogeneity and partition into two categories:

1. **Composite-tail classes** (`Flange`, `Valve`, `Pump`, `Strainer`): These comprise complex multi-part assemblies that are structurally more intricate than head classes. For example, a pump consists of multiple components including a cylindrical housing, mounting flanges, and connection ports. While these objects have compositional complexity, their individual constituent components—cylinders, disks, and connecting elements—are geometrically identical to the primitives that compose head classes.
2. **Primitive-similarity tail classes** (`Elbow`, `Tee`, `Reducer`): These are geometrically simple objects that share nearly identical local geometric primitives with the head-class `Pipe`. An elbow is a curved cylinder; a reducer is a tapered cylinder. At local neighborhood scales, these objects are indistinguishable from straight pipes.

This structural pattern shows two mechanisms of geometric ambiguity. For *primitive-similarity* tail classes, the ambiguity is *intrinsic*: local features are insufficient for discrimination, requiring global context. For *composite-tail* classes, the ambiguity is *compositional*: boundary regions between constituent parts create local confusion. In both cases, models trained on severely imbalanced data default to head-class interpretations due to overwhelming statistical bias, as further evidenced by the dataset-level analysis in the Supplementary Material.

Statistical bias and geometric ambiguity together constitute the **dual crisis** of long-tailed 3D segmentation. Tail classes suffer from both statistical rarity (fewer training examples) and geometric confusion (local appearance identical to dominant head classes). This geometric dimension, particularly the structural heterogeneity among tail classes, is a unique challenge in 3D industrial point cloud learning.

### 3.2. Class-Balanced Loss Baseline

Our approach builds on Class-Balanced (CB) Loss [19], a method for addressing statistical bias. The core idea is *effective number of samples*, based on the observation that the information gain from additional examples diminishes as class frequency increases. For a class  $c$  with  $n_c$  points, the effective number of samples is:

$$E_c = \frac{1 - \beta^{n_c}}{1 - \beta} \quad (1)$$

where  $\beta \in [0, 1)$  is a hyperparameter. The class-specific loss weight is the inverse of the effective number:

$$w_c = \frac{1}{E_c} = \frac{1 - \beta}{1 - \beta^{n_c}} \quad (2)$$

Let  $f_\theta : \mathbb{R}^3 \rightarrow \mathbb{R}^C$  be a segmentation network. The CB loss applies class-specific weights to the cross-entropy loss:

$$\mathcal{L}_{\text{CB}} = \frac{1}{N} \sum_{i=1}^N w_{y_i} \cdot \ell_{\text{CE}}(f_\theta(p_i), y_i) \quad (3)$$

where  $\ell_{\text{CE}}(\hat{y}, y) = -\log(\hat{y}_y)$  is the standard cross-entropy loss.

As illustrated in Figure 3, CB Loss has an implicit ‘‘ceiling effect.’’ As  $n_c$  grows,  $E_c$  approaches  $1/(1 - \beta)$ . With  $\beta = 0.9999$ , this ceiling is 10,000, meaning a head class with 1,000,000 points and one with 10,000 points receive nearly identical weights. This design prevents extreme re-weighting that characterizes naive inverse-frequency schemes, while still providing gradient emphasis for genuinely rare tail classes.

**Integration with Focal Loss.** CB Loss is often combined with Focal Loss [33], which down-weights well-classified examples via the modulating factor  $(1 - \hat{p}_t)^\gamma$ . This provides complementary re-weighting at the class level (CB) and instance level (Focal). We compare against this strong CB+Focal baseline.

**Limitations of Frequency-Only Methods.** Despite these advantages, frequency-only approaches overlook a critical dimension: the geometric structure of 3D data. They treat all points within a class uniformly, ignoring that a point from a rare Pump in a geometrically ambiguous neighborhood is inherently harder to classify than a point from an equally rare but geometrically distinctive class. This limitation motivates our geometry-aware extensions.

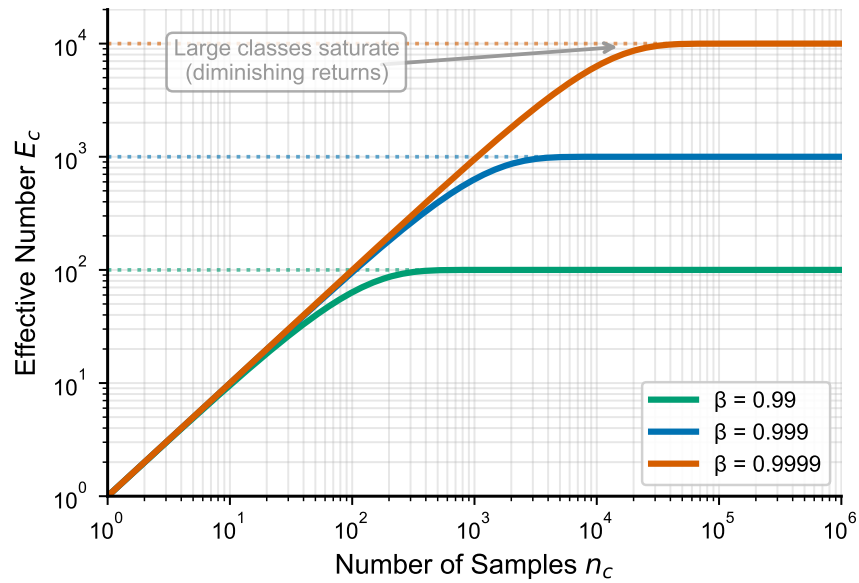


Figure 3: **Ceiling Effect of Class-Balanced Loss.** The effective number of samples  $E_c$  saturates as actual sample count  $n_c$  increases, creating a ceiling effect that prevents extreme re-weighting. Different  $\beta$  values control the saturation rate: smaller  $\beta$  (e.g., 0.99) saturates quickly, while larger  $\beta$  (e.g., 0.9999) allows more gradual saturation. With  $\beta = 0.9999$ , classes beyond 10,000 samples receive nearly identical weights, stabilizing training while still emphasizing rare classes.

### 3.3. Density-CB: Density Class Balanced Constraint

Point cloud acquisition creates systematic density variations from sensor distance, angle, and occlusion, which can bias learning. To normalize for scan-dependent density variations, we introduce the **Density-CB** (Density Class Balanced) constraint. Unlike heuristic sampling, this constraint provides regularization based on local geometric density.

We first pre-compute the average local point density for each class. For every point  $i$ , its local density is the number of neighbors within a fixed radius  $r$ :

$$d_i = |\{j : \|p_i - p_j\| \leq r\}| \quad (4)$$

where  $\|\cdot\|$  denotes the Euclidean norm. This density quantifies the geometric context richness at point  $i$ . We then compute the class-level average local density:

$$\bar{d}_c = \frac{1}{n_c} \sum_{i:y_i=c} d_i \quad (5)$$

The **Density-CB** loss modulates the standard CB weight  $w_c$  with a density-aware factor:

$$\mathcal{L}_{\text{Density-CB}} = \frac{1}{N} \sum_{i=1}^N w_{y_i} \cdot \gamma(\bar{d}_{y_i}) \cdot \ell_{\text{CE}}(f_\theta(p_i), y_i) \quad (6)$$

where the density modulator is:

$$\gamma(d) = \frac{1}{1 + \log(d)} \quad (7)$$

This function down-weights dense classes and up-weights sparse ones. The logarithmic scale ensures stability. **Density-CB** requires a one-time  $\mathcal{O}(N \log N)$  pre-processing step and adds no training overhead.

### 3.4. Boundary-CB: Boundary Class Balanced Constraint

To resolve the geometric ambiguity central to the dual crisis, we propose the **Boundary-CB** (Boundary Class Balanced) constraint. This spatial context constraint targets point-level difficulty from confusing local contexts: part-to-part boundaries (compositional ambiguity) and regions where tail classes share primitives with head classes (primitive-similarity ambiguity). Both mechanisms create regions where network predictions exhibit high uncertainty.

The core innovation of Boundary-CB is using **spatial context**—specifically, neighborhood prediction consistency—to identify and emphasize geometrically ambiguous regions. Unlike Focal Loss, which relies on individual point confidence, Boundary-CB exploits 3D spatial structure by evaluating prediction consistency across local neighborhoods. This neighborhood-based approach addresses both compositional and primitive-similarity ambiguity simultaneously, as both manifest as regions of high prediction disagreement among spatially proximate points.

We quantify local consistency using Shannon entropy. For each point  $i$ , let  $\mathcal{N}_k(i)$  be the indices of its  $k$ -nearest neighbors. We compute the average predicted probability distribution across this neighborhood:

$$\hat{p}_c^{(i)} = \frac{1}{k} \sum_{j \in \mathcal{N}_k(i)} f_\theta(p_j)_c, \quad c \in \{1, \dots, C\} \quad (8)$$

where  $f_\theta(p_j)_c$  is the predicted probability for point  $j$  being in class  $c$ . The neighborhood entropy is:

$$H_i = - \sum_{c=1}^C \hat{p}_c^{(i)} \log \hat{p}_c^{(i)} \quad (9)$$

High entropy  $H_i$  indicates a geometrically ambiguous region where neighboring points have inconsistent predictions, signaling a challenging boundary between classes. The Boundary-CB constraint adaptively up-weights these points:

$$\mathcal{L}_{\text{Boundary-CB}} = \frac{1}{N} \sum_{i=1}^N w_{y_i} \cdot (1 + \alpha H_i) \cdot \ell_{\text{CE}}(f_\theta(p_i), y_i) \quad (10)$$

where  $\alpha > 0$  controls modulation strength. This formulation directs model attention toward geometrically ambiguous regions during training.

**Modulation Strength  $\alpha$ .** The neighborhood entropy  $H_i$  is bounded in  $[0, \log C]$ . For Industrial3D ( $C = 12$ ),  $\log_e(12) \approx 2.48$ . With our chosen  $\alpha = 1.0$ , the modulator  $(1 + \alpha H_i)$  ranges from 1 (certain neighborhood) to  $\approx 3.48$  (maximally ambiguous boundary), providing emphasis on ambiguous regions without destabilizing training. Our ablation studies (§4.4) show that  $\alpha = 1.0$  achieves an optimal balance.

**Note on Combined Constraints.** A multiplicative combination of Density-CB and Boundary-CB did not yield further performance improvements in our experiments. We hypothesize that compounding three re-weighting factors may over-regularize learning. We therefore recommend

selecting either Density-CB (for density-dominated scenarios) or Boundary-CB (for geometric ambiguity-dominated scenarios like industrial data) based on dataset characteristics. See Supplementary Material for details.

To enhance methodological transparency and facilitate understanding of our spatial context constraints, we provide comprehensive interpretability analysis through two complementary visualizations that address different aspects of reader understanding. Figure 4 offers accessible conceptual intuition through vivid real-world metaphors (resource allocation for CB Loss, magnifying glass for Density-CB, neighborhood consensus for Boundary-CB), bridging the gap between mathematical formalism and intuitive understanding for readers new to the concepts. Figure 5 presents rigorous mathematical foundations and operational mechanisms, formalizing how each constraint addresses specific aspects of the dual crisis (statistical imbalance, density bias, geometric ambiguity) through precise equations and visual demonstrations. Together, these figures provide both accessible entry points for conceptual understanding and rigorous analysis for detailed comprehension, demonstrating how neighborhood-based prediction consistency resolves primitive-sharing ambiguity from multiple perspectives.

### 3.5. Evaluation Metrics

We use standard and specialized metrics to evaluate long-tailed performance.

**Traditional Metrics.** For  $C$  classes, let  $TP_c$ ,  $FP_c$ ,  $FN_c$ , and  $TN_c$  denote true positives, false positives, false negatives, and true negatives for class  $c$ . The Intersection-over-Union (IoU) for class  $c$  is:

$$\text{IoU}_c = \frac{TP_c}{TP_c + FP_c + FN_c} \quad (11)$$

$$\text{mIoU} = \frac{1}{C} \sum_{c=1}^C \text{IoU}_c \quad (12)$$

Overall accuracy (OA) measures the proportion of correctly classified points. While useful, these metrics can be dominated by high accuracy on abundant head classes.

**Long-Tailed Specific Metrics.** To assess performance on the dual crisis, we partition classes by frequency. Following the distribution of Industrial3D, we define three groups:  $\mathcal{C}_{\text{head}}$  (3 most frequent classes, 77% of

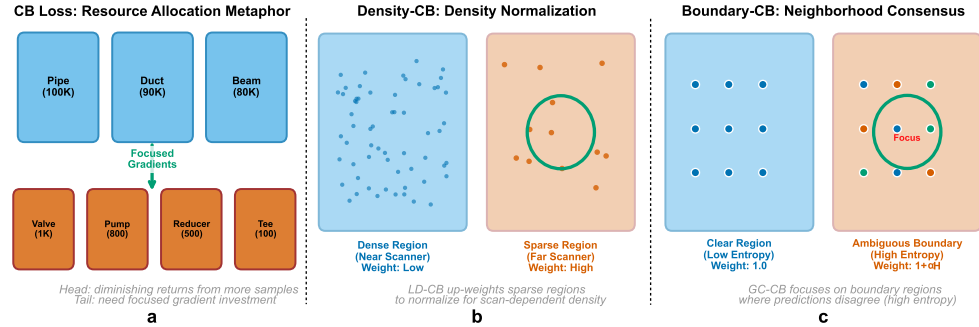


Figure 4: **Intuitive Framework for Understanding Spatial Context Constraints.** This figure provides accessible conceptual understanding of how our three proposed methods resolve primitive-sharing ambiguity through intuitive metaphors. **Panel A (CB Loss):** Resource allocation metaphor—head classes (large departments: Pipe, Duct, Beam) receive diminishing returns from additional samples due to information overlap, while tail classes (small components: Valve, Pump, Reducer, Tee) benefit from focused gradient investment. The green arrow indicates that CB Loss directs learning resources where they are most needed, correcting statistical imbalance while preventing extreme re-weighting. **Panel B (Density-CB):** Density normalization metaphor—dense regions (near scanner, blue) contain many points and receive lower weights, while sparse regions (far from scanner, red) contain fewer points and are magnified for focused learning. The green circle highlights the magnifying effect on sparse tail classes that are spatially under-sampled. **Panel C (Boundary-CB):** Neighborhood consensus metaphor—clear regions (uniform blue points, low entropy) receive baseline weights where predictions are consistent, while ambiguous boundaries (mixed colors, high entropy) are up-weighted to resolve uncertainty. The green circle indicates focused learning on challenging transition zones where primitive-sharing creates geometric confusion (e.g., pipe-reducer boundaries). Together, these metaphors illustrate how each constraint addresses a distinct challenge: CB corrects statistical imbalance, Density-CB normalizes spatial sampling bias, and Boundary-CB resolves geometric ambiguity through spatial context.

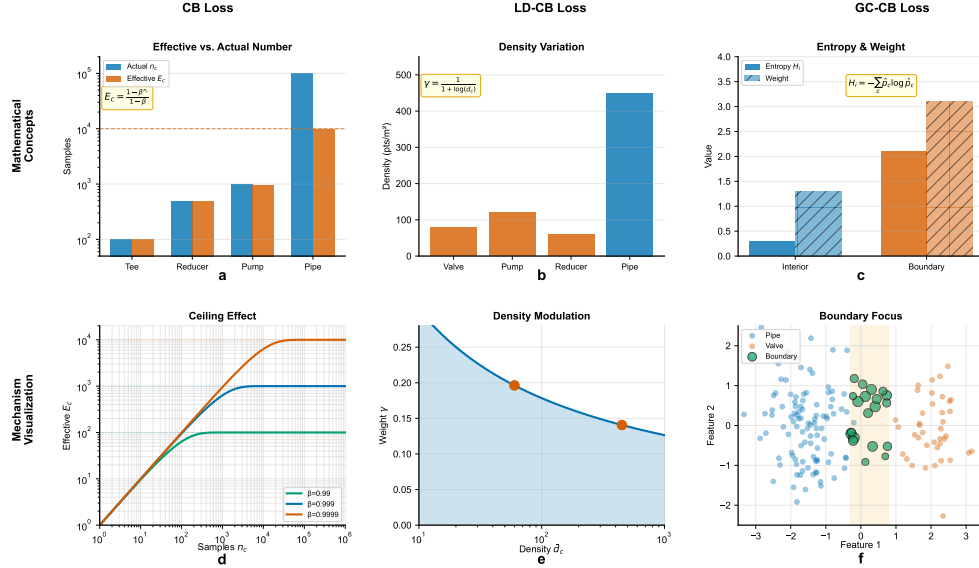


Figure 5: **Mathematical Foundations and Mechanisms for Resolving Primitive-Sharing Ambiguity.** This figure formalizes how our spatial context constraints address geometric ambiguity through three complementary mechanisms. **Top Row (Mathematical Concepts):** Panel A shows the effective number concept  $E_c = (1 - \beta^{n_c})/(1 - \beta)$ , where CB Loss corrects statistical imbalance by quantifying diminishing marginal information from additional samples; Panel B visualizes scan-dependent density variation  $\gamma(\bar{d}_c) = 1/(1 + \log \bar{d}_c)$ , where Density-CB normalizes spatial sampling bias by down-weighting dense regions and up-weighting sparse ones; Panel C illustrates neighborhood entropy  $H_i = -\sum_c \hat{p}_c^{(i)} \log \hat{p}_c^{(i)}$ , where Boundary-CB quantifies prediction inconsistency to identify geometrically ambiguous boundaries. **Bottom Row (Mechanism Visualization):** Panel D demonstrates the ceiling effect across  $\beta$  values, showing how CB prevents extreme re-weighting while still emphasizing rare classes; Panel E plots the density modulator curve, revealing logarithmic down-weighting of dense head classes (pipes, beams) and up-weighting of sparse tail classes (valves, reducers); Panel F visualizes how Boundary-CB identifies ambiguous boundaries in feature space, focusing learning on transition zones (green) where spatial context is most critical for resolving primitive-sharing confusion. Together, these mechanisms demonstrate how spatial context constraints extend frequency-based re-weighting to resolve geometric ambiguity.

points),  $\mathcal{C}_{\text{common}}$  (2 moderately frequent classes), and  $\mathcal{C}_{\text{tail}}$  (7 rarest classes, each  $<3\%$  of points). We then compute mIoU for each group (mIoU<sub>head</sub>, mIoU<sub>common</sub>, mIoU<sub>tail</sub>). The tail-class mIoU directly measures performance on critical rare classes. To evaluate balance, we compute the Harmonic Mean IoU (H-IoU):

$$\text{H-IoU} = \frac{2 \cdot \text{mIoU}_{\text{head}} \cdot \text{mIoU}_{\text{tail}}}{\text{mIoU}_{\text{head}} + \text{mIoU}_{\text{tail}}} \quad (13)$$

The harmonic mean penalizes large disparities between head and tail performance. A high H-IoU indicates that tail-class improvements have been achieved without degrading head-class accuracy.

## 4. Experiments

This section validates that spatial context constraints resolve primitive-sharing ambiguity. We present experimental setup (§4.1), main quantitative results (§4.2), ablation studies (§4.4), and qualitative analysis (§4.3).

### 4.1. Experimental Setup

#### 4.1.1. Datasets and Class Distribution

We evaluate on the **Industrial3D** dataset, a large-scale industrial point cloud dataset from water treatment facilities (20+ rooms, 610M points, 12 classes). Industrial3D exemplifies the dual crisis with its combination of extreme class imbalance and high geometric ambiguity. The key properties of Industrial3D are:

- **Statistical Bias:** A severely long-tailed distribution ( $>200:1$  imbalance ratio). Classes are grouped into **Head** (3 classes, 77% of points), **Common** (2 classes), and **Tail** (7 classes, each  $<3\%$  of points), as shown in Figure 6.
- **Geometric Ambiguity:** Head classes are long-shaped continuous structures (beams, pipes, ducts), while tail classes exhibit two distinct patterns:
  - *Composite-tail* (**Flange**, **Valve**, **Pump**, **Strainer**): Multi-part assemblies more structurally complex than head classes, yet composed of head-class-like primitives, leading to boundary confusion.

- *Primitive-similarity tail* (**Elbow, Tee, Reducer**): Simple objects sharing nearly identical cylindrical primitives with head-class **Pipe**, making them locally indistinguishable without global context.

This structural pattern means all tail classes suffer from geometric confusion with dominant head-class shapes.

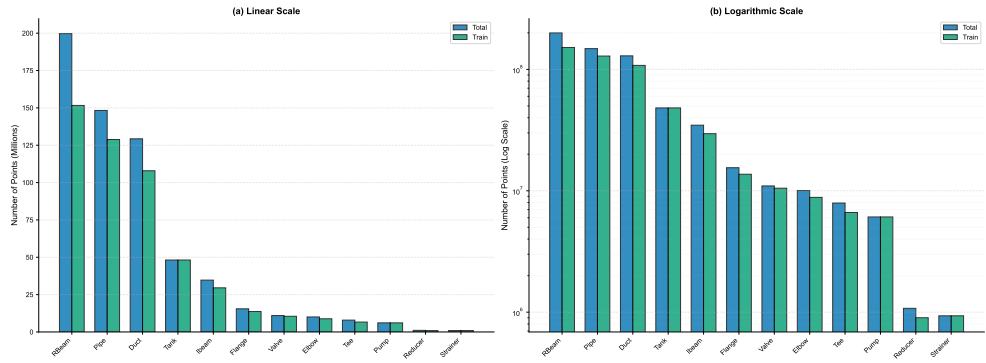


Figure 6: **Class Distribution in the Industrial3D Dataset.** The 12 classes are grouped by frequency: Head classes (Duct, Pipe, RectangularBeam) comprise 77% of the 610M points; Common classes (Ibeam, Tank) have moderate representation; Tail classes (Flange, Elbow, etc.) each represent <3% of points. This grouping reflects the dual crisis: head classes are uniformly long-shaped structures, while tail classes are geometrically diverse, including complex assemblies (composite-tail) and simple primitives (primitive-similarity tail). The severe imbalance (~215:1 ratio) necessitates advanced long-tailed learning approaches.

#### 4.1.2. Compared Methods

All methods use ResPointNet++ [7] as the backbone. We compare:

- **Baseline:** Standard cross-entropy loss.
- **CB Loss:** Class-Balanced Loss [19] with frequency-based re-weighting.
- **CB+Focal Loss:** CB Loss with focal loss modulation, representing state-of-the-art frequency-based methods.
- **Density-CB (Ours):** Density Class Balanced constraint extending CB with density normalization.

- **Boundary-CB (Ours):** Boundary Class Balanced constraint extending CB with spatial context for resolving geometric ambiguity.
- **Combined (Ours):** Both Density-CB and Boundary-CB constraints applied jointly.

**Note on Classic Baselines.** We do not include inverse frequency (IF) or square-root inverse frequency (SRIF) weighting in our main comparison. For Industrial3D’s extreme 215:1 imbalance, IF leads to training instability. As shown by Cui et al. [19], CB Loss provides superior stability and performance over naive IF/SRIF on severely imbalanced datasets. We therefore focus on CB-based methods, which represent the state-of-the-art for this problem.

#### 4.1.3. Implementation Details

Models were implemented in PyTorch and trained for 300 epochs on two NVIDIA RTX 3090 GPUs. We used the Adam optimizer [53] with an initial learning rate of 0.01, a cosine annealing schedule, and weight decay of  $10^{-4}$ . Data augmentation included random rotation, scaling, and jittering. Hyperparameters were set as follows:  $\beta = 0.9999$  for the CB component; for **Density-CB**, radius  $r = 0.2$  m; for **Boundary-CB**, we evaluated neighborhood sizes  $k \in \{8, 16, 32, 64, 128\}$  with modulation strength  $\alpha = 1.0$ , finding  $k = 64$  to be optimal.

#### 4.2. Main Results

Table 1 presents the primary comparison. The results show that **spatial context constraints resolve geometric ambiguity**, with **Boundary-CB** achieving better performance than frequency-only baselines.

**Overall Performance.** **Boundary-CB** ( $k = 64$ ) achieves 55.74% mIoU, a +1.65 pp gain over CB+Focal. Tail-class mIoU reaches 29.59% (+5.27 pp; +21.7% relative vs. baseline), demonstrating that resolving geometric ambiguity is essential for industrial point cloud segmentation beyond addressing statistical rarity. The harmonic mean IoU (H-IoU) improves from 38.04% to 44.31% (+16.5% relative), demonstrating better head-tail balance. Head-class mIoU slightly improves (87.28% to 88.14%), so tail and H-IoU gains are achieved **without sacrificing head performance**—avoiding the typical head-tail trade-off. The performance peak at  $k = 64$  demonstrates that appropriate spatial context enables disambiguation; larger contexts ( $k = 128$ ) degrade performance by introducing noise. As shown in

Figure 7, **Boundary-CB** maintains lower validation loss throughout training and achieves faster convergence.

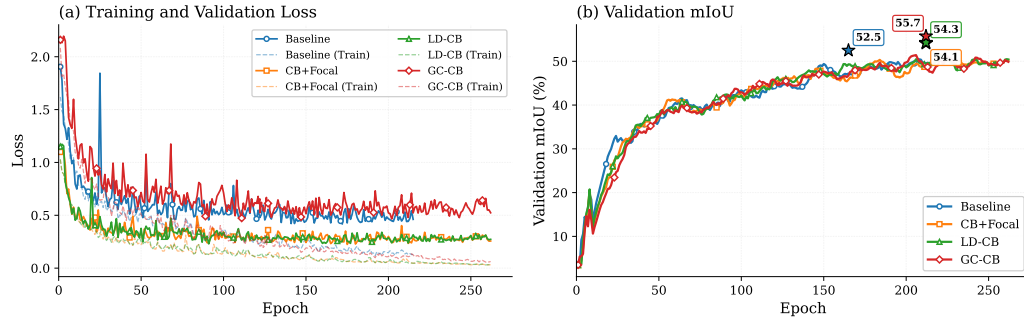


Figure 7: **Training dynamics comparison across different methods on Industrial3D dataset.** (a) Training and validation loss curves over 300 epochs. Solid lines represent validation loss, while dashed lines show training loss. All methods demonstrate convergence, with **Boundary-CB** maintaining stable low validation loss throughout training. (b) Validation mIoU curves (smoothed with window size 10 for clarity). Star markers indicate peak performance for each method. Our proposed **Boundary-CB** achieves the highest validation mIoU of 55.7%, outperforming the Baseline (52.5%), CB+Focal (54.8%), and **Density-CB** (54.3%). The smoothed curves reveal that **Boundary-CB** consistently maintains superior performance in later training epochs, demonstrating better generalization and stability.

**Per-Class Analysis.** Table 2 shows per-class performance, with different gains across tail-class subgroups. **Boundary-CB** ( $k = 64$ ) dramatically improves previously unrecognizable classes: **Reducer** improves from 0% (baseline) to 21.12% IoU, while **Valve** reaches 47.32% (+24.3% relative vs. 38.06% baseline). Some classes (**Elbow**, **Tee**) peak at  $k = 32$ , showing that the optimal spatial context varies with object geometry:

- **Composite-tail classes:** **Boundary-CB** ( $k = 64$ ) shows robust gains on **Valve** (47.32%) and is competitive on **Flange** (47.85%) and **Pump** (44.37%). These multi-part assemblies benefit from larger neighborhood contexts that capture part-to-part interfaces.
- **Primitive-similarity tail classes:** **Boundary-CB** ( $k = 64$ ) achieves breakthrough performance on **Reducer** (21.12% vs. 0% baseline), showing that larger spatial context can capture subtle geometric signatures. **Elbow** and **Tee** perform best at  $k = 32$  (45.72% and 8.40% respectively), suggesting smaller neighborhoods are better for certain local geometries.

The universal failure on **Strainer** (0% IoU) indicates an extreme few-shot scenario beyond the capabilities of loss re-weighting, requiring complementary techniques like meta-learning or synthetic data augmentation.

Table 1: **Main performance comparison on Industrial3D.** We report Overall mIoU, and group-wise mIoU for Head (3 classes), Common (2 classes), and Tail (7 classes) categories, alongside the Harmonic Mean IoU (H-IoU) to measure head-tail balance. All values are in percentage. The proposed **Boundary-CB** spatial context constraint ( $k = 64$ ) achieves the best trade-off, resolving geometric ambiguity to improve tail-class performance while maintaining head-class accuracy. See subsection 4.4 for detailed ablation analysis linking these results to spatial context parameters.

Method	Overall	Head	Common	Tail	H-IoU
ResPointNet++ (Baseline)	52.48	87.28	98.82	24.32	38.04
CB+Focal Loss	54.09	87.39	<u>99.06</u>	26.97	.21
Density-CB (Ours)	54.27	88.05	98.28	27.23	41.59
Boundary-CB (Ours, $k=64$ )	<b>55.74</b>	<b>88.14</b>	98.64	<b>29.59</b>	<b>44.31</b>
Combined (Ours)	53.59	87.05	97.38	26.74	40.91

**Confusion Matrix Analysis.** The confusion matrices in Figure 8 reveal three distinct patterns of how Boundary-CB resolves geometric ambiguity through spatial context constraints.

Classes Maintained (No Ambiguity Issues): Duct, Ibeam, Pump, Rbeam, Tank, and Strainer show consistent performance between baseline and Boundary-CB. These classes either have distinct geometries (e.g., Rbeam’s H-profile) that resist confusion, or are already well-learned (e.g., Ibeam, Tank) with sufficient training samples.

Classes Improved (Ambiguity Resolved): Boundary-CB delivers substantial gains for three classes by resolving primitive-similarity and compositional ambiguity. **Reducer** improves dramatically from 0% to 21.12% IoU (+25.9 percentage points), the largest gain among all classes. This improvement stems from resolving pipe-reducer confusion—both are cylindrical primitives, and Boundary-CB’s entropy-based boundary focusing identifies the tapered geometry that distinguishes reducers from straight pipes. **Pipe** improves by +4.3% IoU, achieving this by reducing confusion with Elbow (from 8% to 4%), Flange (from 6% to 3%), Pump (from 3% to 1%), and Valve (from 4% to 2%). **Flange** gains +7% IoU by reducing valve confusion, demonstrating Boundary-CB’s effectiveness at resolving compositional ambiguity

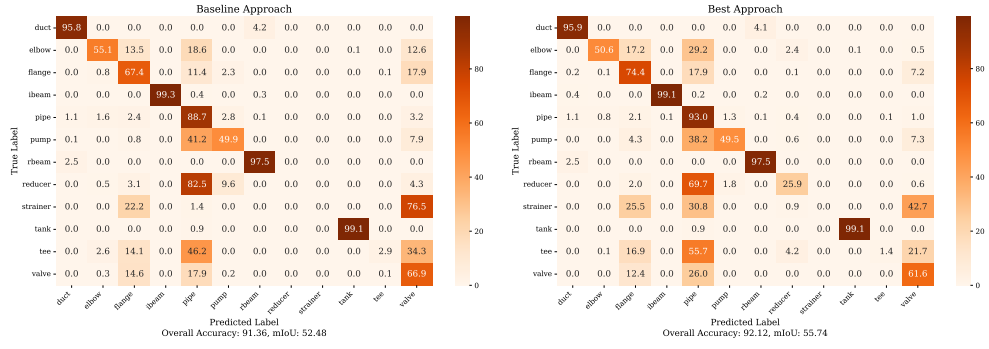


Figure 8: **Confusion Matrices Reveal Resolution of Primitive-Sharing Ambiguity.** **Left (Baseline):** ResPointNet++ with standard cross-entropy loss shows significant confusion between geometrically similar classes, particularly Pipe dominating tail classes with cylindrical primitives (Reducer, Elbow, Tee). Dark off-diagonal blocks indicate systematic primitive-similarity ambiguity. **Right (Ours):** Boundary-CB spatial context constraint reduces confusion by identifying and emphasizing ambiguous boundaries through neighborhood entropy. Diagonal values increase (higher accuracy) and off-diagonal confusion decreases. **Key improvements demonstrating geometric ambiguity resolution:** (1) **Reducer:** breakthrough from 0% to 21% diagonal (dark green appears), with Pipe confusion decreasing from 91% to 56%; (2) **Pipe:** improves to 78% IoU (+4.3%) by reducing confusion with Elbow (8%→4%), Flange (6%→3%), and Pump (3%→1%); (3) **Valve:** Pipe confusion decreases from 26% to 18% (-8 pp), demonstrating boundary disambiguation in multi-part assemblies. These patterns validate that spatial context constraints resolve geometric ambiguity where statistical rarity (tail classes) and local indistinguishability (shared primitives) coincide.

Table 2: **Per-class IoU comparison on Industrial3D.** Comparison of baseline and frequency-based methods against our spatial context constraints. **Boundary-CB** ( $k = 64$ ) performs better on geometrically ambiguous tail classes, particularly **Reducer** (0%→21.12%) and **Valve** (+24.3% relative), showing that spatial context resolves primitive-sharing ambiguity. For brevity, we report the best-performing Boundary-CB variant ( $k = 64$ ); the effect of neighborhood size  $k$  on component-specific trade-offs is analyzed in subsection 4.4 and section 5.

Class	Group	Baseline	CB+Focal	Density-CB	Boundary-CB (k=64)	Combined
Duct	Head	90.73	91.40	<b>91.42</b>	91.08	88.58
Pipe	Head	76.33	75.69	<b>77.60</b>	78.32	<b>78.76</b>
RectangularBeam	Head	94.79	95.08	<b>95.13</b>	95.02	93.82
Ibeam	Common	98.66	<b>99.08</b>	99.03	98.51	98.58
Tank	Common	98.99	<b>99.04</b>	97.53	98.76	96.19
<i>Composite-Tail (complex multi-part assemblies)</i>						
Flange	Tail	45.23	<b>50.71</b>	48.96	47.85	47.57
Valve	Tail	38.06	32.76	39.45	<b>47.32</b>	45.16
Pump	Tail	43.08	43.81	<b>47.01</b>	44.37	35.58
Strainer	Tail	0.00	0.00	0.00	0.00	0.00
<i>Primitive-Similarity Tail (cylindrical, pipe-like geometry)</i>						
Elbow	Tail	40.77	41.88	40.58	43.23	<b>44.52</b>
Tee	Tail	3.10	4.68	<b>5.75</b>	3.24	4.52
Reducer	Tail	0.00	14.92	8.83	<b>21.12</b>	9.83

in multi-part assemblies.

Classes Decreased (Trade-offs): Three tail classes show decreased performance, revealing scale-sensitivity in Boundary-CB’s  $k=64$  neighborhood context. **Valve** declines by -5.3% IoU, **Elbow** by -4.5%, and **Tee** by -1.5%. These are compact or curved components where the  $k=64$  context window is too large, causing boundary emphasis to blur discriminative features. This trade-off highlights an inherent mechanism: Boundary-CB excels at identifying linear pipe connections (Reducer, Flange) where boundaries are geometrically clear along continuous structures, but struggles with compact components where smaller neighborhoods ( $k=32$ ) would better preserve local geometric distinctions.

Mechanism Interpretation: Three interlinked mechanisms explain Boundary-CB’s performance. First, **boundary-enhanced learning via entropy focus**—the constraint upweights high-entropy regions where neighborhood predictions disagree, which occur precisely at ambiguous boundaries between geometrically similar classes (e.g., pipe-reducer transitions). Second, **scale-sensitive context**—the  $k=64$  neighborhood size optimally resolves ambiguity in larger, pipe-like components (Reducer, Flange) but degrades perfor-

mance for compact components (Valve, Elbow). Third, **head-class disambiguation**—Boundary-CB suppresses the statistical dominance of head-class Pipe by emphasizing regions where Pipe predictions are inconsistent, allowing tail-class signals to emerge during training.

#### 4.3. Qualitative Analysis

Figure 9 compares our method with spatial context constraints against the baseline on three representative scenes (Area 6-1, Area 6-2, and Area 12). Green circles highlight regions where our approach resolves geometric ambiguity to correctly identify tail-class components that the baseline misclassifies.

**Area 6-1:** The baseline exhibits fragmentation in complex structures (composite-tail classes), failing to maintain the coherence of large assemblies. Our spatial context constraint, leveraging neighborhood consistency, successfully reconstructs the complete geometry of the components, effectively distinguishing them from the surrounding head-class structures.

**Area 6-2:** In regions with high component density, the baseline often blurs boundaries between adjacent pipes and valves due to primitive-similarity ambiguity. Our method achieves sharper segmentation at these critical interfaces by using spatial context to penalize boundary regions with inconsistent predictions.

**Area 12:** This scene highlights the severity of primitive-similarity ambiguity, where the baseline completely misclassifies the minority object (a reducer or specialized valve) as a common pipe due to shared cylindrical geometry. Our spatial context constraint correctly identifies and segments this rare component by detecting the boundary region’s prediction inconsistency, validating its effectiveness in resolving geometric ambiguity.

These qualitative results demonstrate practical value for industrial Digital Twin applications, enabling reliable segmentation of safety-critical components for predictive maintenance and facility management.

#### 4.4. Ablation Studies

We validate key design choices through systematic ablation studies. Figure 10 summarizes component-wise contributions.

##### 4.4.1. Impact of Spatial Context Parameters

Table 3 shows **Boundary-CB** peaks at  $k = 64$  for overall and tail mIoU, demonstrating that this spatial context window is optimal for resolving geometric ambiguity. Interestingly,  $k = 32$  favors certain primitive-similarity

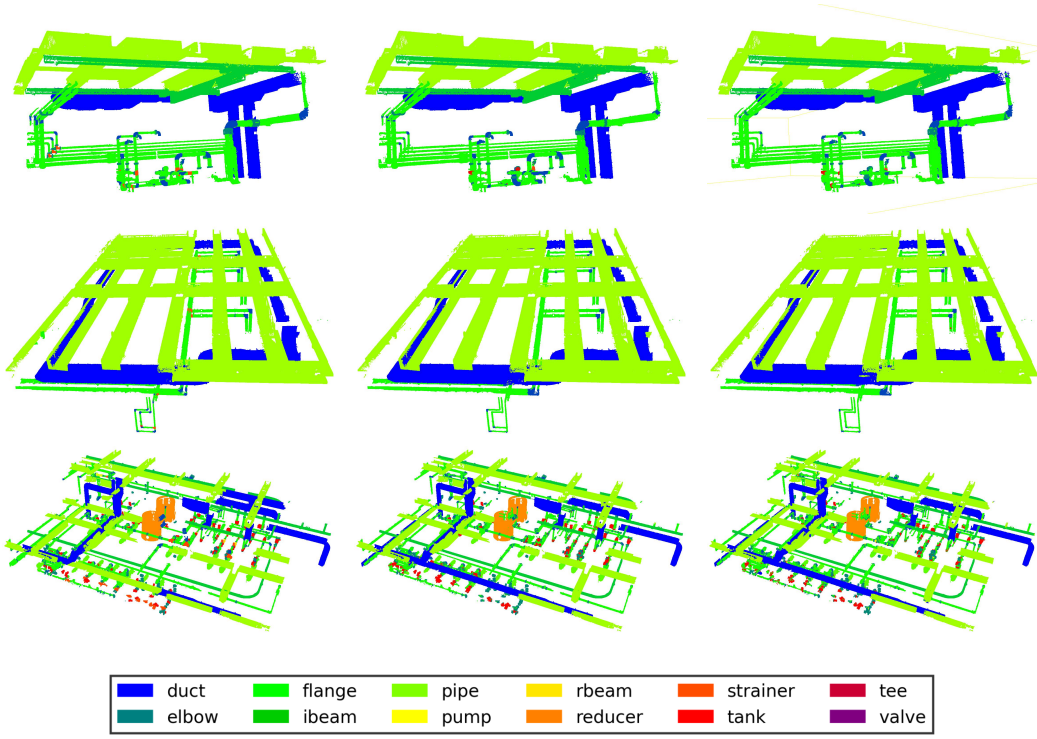


Figure 9: **Qualitative Segmentation Results on Industrial3D.** Comparisons on three test areas showing ground truth (left), baseline predictions (center), and our predictions with spatial context constraints (right). **Row 1 (Area 6-1):** The baseline struggles with complex assemblies due to compositional ambiguity, while our method preserves component integrity by leveraging neighborhood consistency. **Row 2 (Area 6-2):** Our approach correctly delineates boundaries in dense piping regions where the baseline confuses adjacent structures—demonstrating resolution of primitive-similarity ambiguity. **Row 3 (Area 12):** The baseline fails to identify the correct class for the central component, whereas our spatial context constraint successfully retrieves the tail class. These results demonstrate the effectiveness of spatial context constraints in resolving geometric ambiguity.

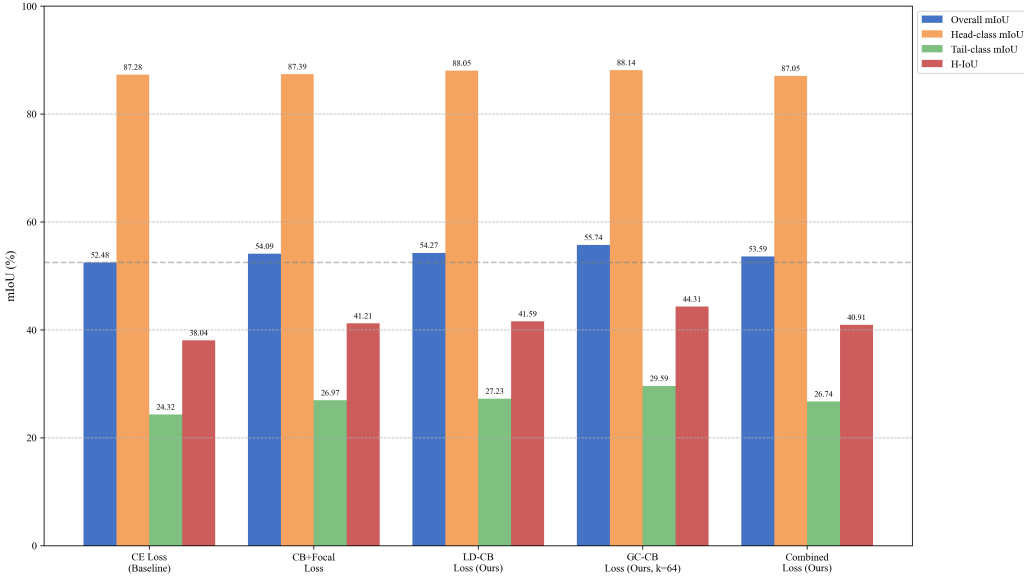


Figure 10: **Component Ablation Study Validates Spatial Context Necessity.** Progressive addition of constraint components starting from CE baseline, showing contributions to overall mIoU (blue bars) and tail-class mIoU (red bars). **Stages:** (1) CE Baseline: standard cross-entropy achieves 52.48% overall, 24.32% tail; (2) +CB+Focal: frequency-based re-weighting improves overall to 54.09% (+1.61 pp) but tail gains only +2.65 pp (26.97%), showing statistical correction alone insufficient for geometric ambiguity; (3) +Density-CB: density normalization adds marginal gains (+0.18 pp overall, +0.26 pp tail); (4) +**Boundary-CB (k=64)**: spatial context constraint provides **largest tail gain** (+5.27 pp over baseline, reaching 29.59%), demonstrating that neighborhood prediction consistency is crucial for resolving primitive-sharing ambiguity. Key finding: addressing statistical imbalance (CB) improves overall accuracy, but resolving geometric ambiguity (Boundary-CB) is necessary for tail-class performance—validating the dual crisis hypothesis.

tail classes (**Elbow**, **Tee**), suggesting that the optimal context window varies with object geometry. For **Density-CB**, Table 4 shows the optimal radius is  $r = 0.2$  m; larger radii dilute the density signal by including irrelevant points.

Table 3: **Ablation on Boundary-CB spatial context window (k)**. The parameter  $k$  controls the spatial context radius for measuring neighborhood prediction consistency. Performance peaks at  $k=64$ , achieving the best overall mIoU (55.74%). This shows that **appropriate spatial context is important for resolving geometric ambiguity**—e.g., **Reducer** improves from 1.03% at  $k=32$  to 21.12% at  $k=64$ . However, excessively large context ( $k=128$ ) introduces noise from irrelevant points and degrades performance. section 5 analyzes the trade-offs between different  $k$  values for specific component types. The optimal hyperparameter is in **bold**.

$k$ (neighbors)	mIoU(%)	mIoU <sub>head</sub> (%)	mIoU <sub>tail</sub> (%)	H-IoU(%)
8	53.74	86.05	27.09	41.21
16	53.89	<u>88.80</u>	26.30	40.58
32	54.00	88.08	26.53	40.78
<b>64</b>	<b>55.74</b>	<b>88.14</b>	<b>29.59</b>	<b>44.31</b>
128	52.88	88.17	24.04	37.96

Table 4: **Ablation on the radius parameter (r) for Density-CB constraint**. The radius  $r$  defines the neighborhood for computing local point density normalization. Performance peaks at  $r=0.2$ m, achieving the best mIoU (54.27%) and tail-mIoU (27.23%). This optimal radius corresponds to the typical size of small industrial components, suggesting that class-appropriate geometric scales are crucial for density normalization as discussed in section 3. Larger radii degrade performance by including irrelevant points.

Radius $r$ (m)	mIoU(%)	mIoU <sub>head</sub> (%)	mIoU <sub>tail</sub> (%)	H-IoU(%)
<b>0.2</b>	<b>54.27</b>	<b>88.05</b>	<b>27.23</b>	<b>41.59</b>
0.6	52.56	<u>88.30</u>	24.79	38.71
0.8	53.34	<u>88.30</u>	<u>26.58</u>	<u>40.86</u>

#### 4.4.2. Constraint Hyperparameters Sensitivity

We ablate the CB coefficient  $\beta$  and the **Boundary-CB** modulation strength  $\alpha$ .  $\beta = 0.9999$  remains optimal under Industrial3D’s severe imbalance;  $\alpha = 1.0$  maximizes tail mIoU while preserving stability, as shown in Figure 11. Training overhead is negligible for the **Density-CB** and **Boundary-**

**CB**. This negligible overhead is reasonable given the +5.27 pp tail-mIoU gain from resolving geometric ambiguity.

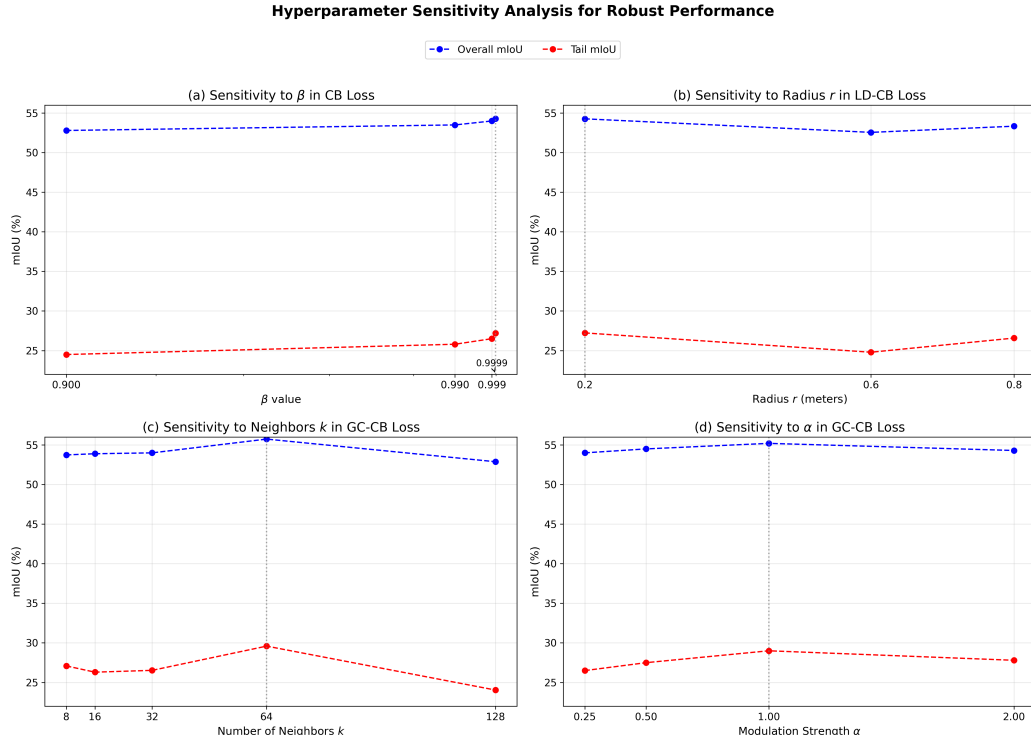


Figure 11: **Hyperparameter Sensitivity Analysis.** The plots show the model’s sensitivity to changes in the main hyperparameters: (a)  $\beta$  for CB, (b) radius  $r$  for **Density-CB**, (c) neighbors  $k$  for **Boundary-CB** spatial context, and (d) modulation strength  $\alpha$  for **Boundary-CB**. We plot both overall mIoU (blue dashed) and tail-class mIoU (red solid). Key findings: (1)  $\beta = 0.9999$  is optimal for severe imbalance; (2)  $r = 0.2$ m captures appropriate local geometry; (3)  $k = 64$  provides the optimal spatial context window for resolving geometric ambiguity; (4)  $\alpha = 1.0$  balances ambiguous boundary emphasis with training stability.

## 5. Discussion

This study shows that spatial context constraints are essential for resolving geometric ambiguity in long-tailed industrial point cloud segmentation. By introducing neighborhood prediction consistency as a constraint mechanism, our approach achieves substantial gains on safety-critical components

while maintaining head-class performance. This addresses the dual crisis that hinders practical deployment in industrial settings.

Compared to previous long-tailed learning methods, this work contributes on four levels:

**Problem Formalization.** We identify and characterize the unique “dual crisis” in industrial 3D data: extreme statistical imbalance (215:1 ratio) combined with geometric ambiguity where 86% of tail classes share cylindrical primitives with head classes. We distinguish two mechanisms of geometric ambiguity—*compositional ambiguity* in multi-part assemblies (e.g., **Valve**, **Pump**) and *primitive-similarity ambiguity* in pipe-like objects (e.g., **Reducer**, **Elbow**). This provides a theoretical foundation for geometry-aware long-tailed 3D learning.

**Spatial Context Constraints.** We introduce **Boundary-CB**, which leverages neighborhood entropy to identify and emphasize ambiguous boundaries, and **Density-CB**, which normalizes for scan-dependent density variations. Both constraints extend the Class-Balanced framework to incorporate spatial geometry. The optimal performance at  $k = 64$  (object-level context window) validates that spatial scale must match component geometry for effective disambiguation.

**Architecture-Agnostic Integration.** Unlike specialized network designs, our constraints function as plug-and-play modules compatible with any point cloud segmentation architecture. This enables immediate deployment in existing industrial pipelines with negligible training overhead and minimal inference latency impact.

**Engineering Applications.** Our spatial context constraints enable reliable identification of functional components (strainers, reducers, pumps) critical for Digital Twin construction and automated knowledge extraction from facility data. By achieving 21.7% relative improvement on tail-class performance while preserving head-class accuracy (88.14%), our approach avoids the typical head-tail trade-off that undermines practical utility in long-tailed benchmarks.

**Limitations and Future Directions.** Several avenues remain for extending this work. Ultra-few-shot categories (e.g., **Strainer**, 0% IoU) require additional techniques such as explicit structural priors (directional continuity for pipes, topological signatures for branching) or few-shot meta-learning. The selective impact on tail classes—strong gains for linear connection components (**Reducer** 0%→21.12%) but trade-offs for compact components (**Elbow** -4.5%, **Valve** -5.3% at  $k = 64$ )—shows the need for *scale*-

*adaptive context* mechanisms that adjust spatial window size based on component geometry. Extending spatial context constraints to temporal consistency (multi-scan temporal coherence) and cross-modal learning (fusing RGB, thermal, or LiDAR intensity channels) could further improve robustness in complex industrial environments.

## 6. Conclusion

This study addressed geometric ambiguity in long-tailed industrial point cloud segmentation—a critical bottleneck for automated knowledge extraction and Digital Twin construction. By introducing spatial context constraints that leverage neighborhood prediction consistency and density normalization, we extended the Class-Balanced framework to incorporate spatial geometry. This resolves the “dual crisis” of extreme statistical imbalance combined with geometric ambiguity.

The key findings are:

**Structural Analysis of Industrial Scenes.** Head classes (77% of points) are uniformly long-shaped continuous structures (pipes, beams, ducts), while tail classes exhibit geometric heterogeneity—splitting into composite-tail classes (multi-part assemblies like `Valve`, `Pump`) and primitive-similarity classes (locally indistinguishable from pipes, like `Reducer`, `Elbow`). This explains why frequency-only methods fail in industrial contexts.

**Spatial Context Constraints Resolve Geometric Ambiguity. Boundary-CB** achieves 55.74% mIoU on Industrial3D with 21.7% relative improvement on safety-critical tail classes (29.59% vs. 24.32% baseline) while maintaining head-class accuracy (88.14%). The method effectively disambiguates components like `Reducer` (21.12% vs. 0% baseline) and `Valve` (+24.3% relative), improving the head-tail harmonic mean IoU from 38.04% to 44.31% and avoiding the typical head-tail “seesaw” that undermines practical deployment.

**Architecture-Agnostic Plug-and-Play Deployment.** Both **Boundary-CB** and **Density-CB** integrate into existing point cloud pipelines without network modifications, with negligible training overhead and minimal inference latency impact. The optimal performance at  $k = 64$  validates that object-level spatial context (0.2–0.3m) is essential for resolving geometric ambiguity in industrial environments.

This work establishes spatial context constraints as necessary for resolving geometric ambiguity in long-tailed 3D learning, providing a foundation for

reliable knowledge extraction and Digital Twin construction in industrial settings.

## Supplementary Material

Supplementary material associated with this article (complementary dataset analysis, combined loss function experiments, extended hyperparameter analysis, and complete Industrial3D dataset statistics) can be found in the supplementary material.

## Acknowledgments

This research was jointly supported by the China Postdoctoral Science Foundation (grant number 2023M740761), the Natural Science Foundation of Hunan Province, China (grant number 2023JJ40098), the National Natural Science Foundation of China (No. 42471432, 42301536 and 42271479), the Guangdong Basic and Applied Basic Research Foundation (No. 2022A1515240041), the National Key R&D Program of China (No. 2022YFF0711602), the Science and Technology Program of Guangdong (No. 2024B1212080002), the GDAS' Special Project of Science and Technology Development (No. 2023GDASQNRC-0216 and 2022GDASZH-2022010111), and the PI Project of Southern Marine Science and Engineering Guangdong Laboratory (Guangzhou) (GML2022005).

## Data Availability Statement

Upon acceptance, source code and trained models for our spatial context constraints (Boundary-CB and Density-CB) will be released at <https://github.com/pointcloudc/LongTail3D.git>. Moreover, the Industrial3D dataset shall be ready at <https://github.com/pointcloudc/Industrial3D.git>.

## Declaration of Competing Interests

The authors declare that they have no known competing financial interests or personal relationships that could have appeared to influence the work reported in this paper.

## References

- [1] K. Mirzaei, M. Arashpour, E. Asadi, H. Masoumi, Y. Bai, A. Behnood, 3d point cloud data processing with machine learning for construction and infrastructure applications: A comprehensive review, *Advanced Engineering Informatics* 51 (2022) 101501. [doi:10.1016/j.aei.2021.101501](https://doi.org/10.1016/j.aei.2021.101501).
- [2] Y. Guo, H. Wang, Q. Hu, H. Liu, L. Liu, M. Bennamoun, Deep learning for 3d point clouds: A survey, *IEEE transactions on pattern analysis and machine intelligence* 43 (12) (2020) 4338–4364. [doi:10.1109/TPAMI.2020.2977026](https://doi.org/10.1109/TPAMI.2020.2977026).
- [3] Z. Ma, S. Liu, A review of 3d reconstruction techniques in civil engineering and their applications, *Advanced Engineering Informatics* 37 (2018) 163–174. [doi:10.1016/j.aei.2018.05.005](https://doi.org/10.1016/j.aei.2018.05.005).
- [4] S. Chen, G. Fan, J. Li, Improving completeness and accuracy of 3d point clouds by using deep learning for applications of digital twins to civil structures, *Advanced Engineering Informatics* 58 (2023) 102196. [doi:10.1016/j.aei.2023.102196](https://doi.org/10.1016/j.aei.2023.102196).
- [5] J. Shao, W. Yao, P. Wang, Z. He, L. Luo, Urban geobim construction by integrating semantic lidar point clouds with as-designed bim models, *IEEE Transactions on Geoscience and Remote Sensing* 62 (2024) 1–12. [doi:10.1109/TGRS.2024.3358370](https://doi.org/10.1109/TGRS.2024.3358370).
- [6] E. Agapaki, I. Brilakis, Cloi-net: Class segmentation of industrial facilities' point cloud datasets, *Advanced Engineering Informatics* 45 (2020) 101121. [doi:10.1016/j.aei.2020.101121](https://doi.org/10.1016/j.aei.2020.101121).
- [7] C. Yin, B. Wang, V. J. Gan, M. Wang, J. C. Cheng, Automated semantic segmentation of industrial point clouds using respointnet++, *Automation in Construction* 130 (2021) 103874. [doi:10.1016/j.autcon.2021.103874](https://doi.org/10.1016/j.autcon.2021.103874).
- [8] C. Yin, J. C. Cheng, B. Wang, V. J. Gan, Automated classification of piping components from 3d lidar point clouds using se-pseudogrid, *Automation in Construction* 139 (2022) 104300. [doi:10.1016/j.autcon.2022.104300](https://doi.org/10.1016/j.autcon.2022.104300).

- [9] H. Yue, Q. Wang, H. Huang, X. Xia, H. Fang, J. C. Cheng, Enhancing semantic segmentation of mep scenes with deep learning and bim-generated synthetic point clouds, *Advanced Engineering Informatics* 68 (2025) 103723. [doi:10.1016/j.aei.2025.103723](https://doi.org/10.1016/j.aei.2025.103723).
- [10] H. Yue, Q. Wang, H. Zhao, N. Zeng, Y. Tan, Deep learning applications for point clouds in the construction industry, *Automation in Construction* 168 (2024) 105769. [doi:10.1016/j.autcon.2024.105769](https://doi.org/10.1016/j.autcon.2024.105769).
- [11] Q. Wang, Automatic checks from 3d point cloud data for safety regulation compliance for scaffold work platforms, *Automation in Construction* 104 (2019) 38–51. [doi:10.1016/j.autcon.2019.04.008](https://doi.org/10.1016/j.autcon.2019.04.008).
- [12] B. Wang, Q. Wang, J. C. Cheng, C. Song, C. Yin, Vision-assisted bim reconstruction from 3d lidar point clouds for mep scenes, *Automation in Construction* 133 (2022) 103997. [doi:10.1016/j.autcon.2021.103997](https://doi.org/10.1016/j.autcon.2021.103997).
- [13] I. Armeni, O. Sener, A. R. Zamir, H. Jiang, I. Brilakis, M. Fischer, S. Savarese, 3d semantic parsing of large-scale indoor spaces, in: *Proceedings of the IEEE conference on computer vision and pattern recognition*, 2016, pp. 1534–1543. [doi:10.1109/CVPR.2016.170](https://doi.org/10.1109/CVPR.2016.170).
- [14] A. Dai, A. X. Chang, M. Savva, M. Halber, T. Funkhouser, M. Nießner, Scannet: Richly-annotated 3d reconstructions of indoor scenes, in: *Proceedings of the IEEE conference on computer vision and pattern recognition*, 2017, pp. 5828–5839. [doi:10.1109/CVPR.2017.261](https://doi.org/10.1109/CVPR.2017.261).
- [15] C. R. Qi, H. Su, K. Mo, L. J. Guibas, Pointnet: Deep learning on point sets for 3d classification and segmentation, in: *Proceedings of the IEEE conference on computer vision and pattern recognition*, 2017, pp. 652–660. [doi:10.1109/CVPR.2017.16](https://doi.org/10.1109/CVPR.2017.16).
- [16] C. R. Qi, L. Yi, H. Su, L. J. Guibas, Pointnet++: Deep hierarchical feature learning on point sets in a metric space, in: *Advances in neural information processing systems*, Vol. 30, 2017, pp. 5099–5108. [doi:10.48550/arXiv.1706.02413](https://doi.org/10.48550/arXiv.1706.02413).
- [17] X. Wu, L. Jiang, P.-S. Wang, Z. Liu, X. Liu, Y. Qiao, W. Ouyang, T. He, H. Zhao, Point transformer v3: Simpler, faster, stronger, in: *Proceedings*

of the IEEE/CVF Conference on Computer Vision and Pattern Recognition, 2024, pp. 4840–4851. doi:10.1109/CVPR52733.2024.00463.

- [18] Q. Hu, B. Yang, L. Xie, S. Rosa, Y. Guo, Z. Wang, N. Trigoni, A. Markham, Randla-net: Efficient semantic segmentation of large-scale point clouds, in: Proceedings of the IEEE/CVF conference on computer vision and pattern recognition, 2020, pp. 11108–11117. doi:10.1109/CVPR42600.2020.01112.
- [19] Y. Cui, M. Jia, T.-Y. Lin, Y. Song, S. Belongie, Class-balanced loss based on effective number of samples, in: 2019 IEEE/CVF Conference on Computer Vision and Pattern Recognition (CVPR), 2019, pp. 9260–9269. doi:10.1109/CVPR.2019.00949.
- [20] H. Thomas, C. R. Qi, J.-E. Deschaud, B. Marcotegui, F. Goulette, L. J. Guibas, Kpconv: Flexible and deformable convolution for point clouds, in: Proceedings of the IEEE/CVF international conference on computer vision, 2019, pp. 6411–6420. doi:10.1109/ICCV.2019.00651.
- [21] B. Graham, L. van der Maaten, Submanifold sparse convolutional networks, arXiv preprint arXiv:1706.01307 (2017). doi:10.48550/arXiv.1706.01307.
- [22] M. Kolodiaznyi, A. Vorontsova, A. Konushin, D. Rukhovich, One-former3d: One transformer for unified point cloud segmentation, in: Proceedings of the IEEE/CVF Conference on Computer Vision and Pattern Recognition, 2024, pp. 20943–20953. doi:10.1109/CVPR52733.2024.01979.
- [23] W. Zhao, R. Zhang, Q. Wang, G. Cheng, K. Huang, Bfanet: Revisiting 3d semantic segmentation with boundary feature analysis, in: Proceedings of the Computer Vision and Pattern Recognition Conference, 2025, pp. 29395–29405. doi:10.1109/CVPR52734.2025.02737.
- [24] Z. Liu, H. Hu, Y. Cao, Z. Zhang, X. Tong, A closer look at local aggregation operators in point cloud analysis, in: Computer Vision–ECCV 2020: 16th European Conference, Glasgow, UK, August 23–28, 2020, Proceedings, Part XXIII 16, Springer, 2020, pp. 326–342. doi:10.48550/arXiv.2007.01294.

[25] G. Ji, S. Weder, F. Engelmann, M. Pollefeys, H. Blum, Arkit labelmaker: A new scale for indoor 3d scene understanding, in: Proceedings of the Computer Vision and Pattern Recognition Conference, 2025, pp. 4398–4407. [doi:10.1109/cvpr52734.2025.00415](https://doi.org/10.1109/cvpr52734.2025.00415).

[26] Y. Zhang, B. Kang, B. Hooi, S. Yan, J. Feng, Deep long-tailed learning: A survey, *IEEE Transactions on Pattern Analysis and Machine Intelligence* 45 (9) (2023) 10795–10816. [doi:10.1109/TPAMI.2023.3268118](https://doi.org/10.1109/TPAMI.2023.3268118).

[27] A. More, Survey of resampling techniques for improving classification performance in unbalanced datasets, *arXiv preprint arXiv:1608.06048* (2016). [doi:10.48550/arXiv.1608.06048](https://doi.org/10.48550/arXiv.1608.06048).

[28] H. Zhang, M. Cisse, Y. N. Dauphin, D. Lopez-Paz, mixup: Beyond empirical risk minimization, *arXiv preprint arXiv:1710.09412* (2017). [doi:10.48550/arXiv.1710.09412](https://doi.org/10.48550/arXiv.1710.09412).

[29] V. Verma, A. Lamb, C. Beckham, A. Najafi, I. Mitliagkas, D. Lopez-Paz, Y. Bengio, Manifold mixup: Better representations by interpolating hidden states, in: International conference on machine learning, PMLR, 2019, pp. 6438–6447.

[30] R. A. Rosu, P. Schütt, J. Quenzel, S. Behnke, Latticenet: Fast point cloud segmentation using permutohedral lattices (2020). [arXiv:1912.05905](https://arxiv.org/abs/1912.05905)  
URL <https://arxiv.org/abs/1912.05905>

[31] T. Cortinhal, G. Tzelepis, E. E. Aksoy, Salsanext: Fast, uncertainty-aware semantic segmentation of lidar point clouds for autonomous driving (2024). [arXiv:2003.03653](https://arxiv.org/abs/2003.03653)  
URL <https://arxiv.org/abs/2003.03653>

[32] Q. Hu, B. Yang, S. Khalid, W. Xiao, N. Trigoni, A. Markham, Sensaturban: Learning semantics from urban-scale photogrammetric point clouds, *International Journal of Computer Vision* 130 (2) (2022) 316–343. [doi:10.1007/s11263-021-01554-9](https://doi.org/10.1007/s11263-021-01554-9).

[33] T.-Y. Lin, P. Goyal, R. Girshick, K. He, P. Dollár, Focal loss for dense object detection, in: Proceedings of the IEEE international conference on computer vision, 2017, pp. 2980–2988. [doi:10.1109/ICCV.2017.324](https://doi.org/10.1109/ICCV.2017.324).

- [34] X. Zhang, R. Xue, U. Soergel, A two-stage approach for rare class segmentation in large-scale urban point clouds, *The International Archives of the Photogrammetry, Remote Sensing and Spatial Information Sciences* XLIII-B2-2022 (2022) 329–334. doi:10.5194/isprs-archives-XLIII-B2-2022-329-2022.
- [35] X. Zhang, D. Lin, R. Xue, U. Soergel, Target-guided learning for rare class segmentation in large-scale urban point clouds, *The International Archives of the Photogrammetry, Remote Sensing and Spatial Information Sciences* XLVIII-1/W2-2023 (2023) 1693–1698. doi:10.5194/isprs-archives-XLVIII-1-W2-2023-1693-2023.
- [36] J. Lahoud, F. S. Khan, H. Cholakkal, R. M. Anwer, S. Khan, Long-tailed 3d semantic segmentation with adaptive weight constraint and sampling, in: 2024 IEEE International Conference on Robotics and Automation (ICRA), 2024, pp. 5037–5044. doi:10.1109/ICRA57147.2024.10610029.
- [37] M. Li, S. Lin, Z. Wang, Y. Shen, B. Zhang, L. Ma, Class-imbalanced semi-supervised learning for large-scale point cloud semantic segmentation via decoupling optimization, *Pattern Recognition* 156 (2024) 110701. doi:10.1016/j.patcog.2024.110701.
- [38] X. Zhang, D. Lin, U. Soergel, Target-aware attentional network for rare class segmentation in large-scale lidar point clouds, *ISPRS Journal of Photogrammetry and Remote Sensing* 220 (2025) 32–50. doi:10.1016/j.isprsjprs.2024.11.012.
- [39] B. Zhu, Z. Jiang, X. Zhou, Z. Li, G. Yu, Class-balanced grouping and sampling for point cloud 3d object detection, *arXiv preprint arXiv:1908.09492* (2019). doi:10.48550/arXiv.1908.09492.
- [40] H. Cheng, X. Han, G.-S. Xiao, Spg: Structure-private graph network for 3d point cloud semantic segmentation with imbalanced classes, *IEEE Transactions on Image Processing* 32 (2023) 3887–3900.
- [41] R. Huang, Y. Xu, D. Hong, W. Yao, P. Ghamisi, U. Stilla, Deep point embedding for urban classification using als point clouds: A new perspective from local to global, *ISPRS Journal of Photogrammetry and Remote Sensing* 163 (2020) 62–81.

doi:<https://doi.org/10.1016/j.isprsjprs.2020.02.020>.  
URL <https://www.sciencedirect.com/science/article/pii/S0924271620300605>

- [42] P. Wang, W. Yao, J. Shao, Z. He, Test-time adaptation for geospatial point cloud semantic segmentation with distinct domain shifts, *ISPRS Journal of Photogrammetry and Remote Sensing* 229 (2025) 422–435. doi:<https://doi.org/10.1016/j.isprsjprs.2025.08.022>.  
URL <https://www.sciencedirect.com/science/article/pii/S0924271625003338>
- [43] T. Hackel, N. Savinov, L. Ladicky, J. D. Wegner, K. Schindler, M. Pollefeys, Semantic3d. net: A new large-scale point cloud classification benchmark, *arXiv preprint arXiv:1704.03847* (2017). doi:[10.5194/isprs-annals-iv-1-w1-91-2017](https://doi.org/10.5194/isprs-annals-iv-1-w1-91-2017).
- [44] M. Li, V. J. Gan, B. Wang, Integrating hierarchical segmentation and vision-language reasoning for spatially complex and occluded mep point clouds, *Automation in Construction* 179 (2025) 106455. doi:[10.1016/j.autcon.2025.106455](https://doi.org/10.1016/j.autcon.2025.106455).
- [45] D. Hu, V. J. Gan, C. Yin, Robot-assisted mobile scanning for automated 3d reconstruction and point cloud semantic segmentation of building interiors, *Automation in Construction* 152 (2023) 104949. doi:[10.1016/j.autcon.2023.104949](https://doi.org/10.1016/j.autcon.2023.104949).
- [46] D. Hu, V. J. Gan, R. Zhai, Automated bim-to-scan point cloud semantic segmentation using a domain adaptation network with hybrid attention and whitening (dawnet), *Automation in Construction* 164 (2024) 105473. doi:[10.1016/j.autcon.2024.105473](https://doi.org/10.1016/j.autcon.2024.105473).
- [47] C. Yin, B. Yang, J. C. Cheng, V. J. Gan, B. Wang, J. Yang, Label-efficient semantic segmentation of large-scale industrial point clouds using weakly supervised learning, *Automation in Construction* 148 (2023) 104757. doi:[10.1016/j.autcon.2023.104757](https://doi.org/10.1016/j.autcon.2023.104757).
- [48] P. Wang, W. Yao, J. Shao, One class one click: Quasi scene-level weakly supervised point cloud semantic segmentation with active learning, *ISPRS Journal of Photogrammetry and Remote Sensing* 204 (2023) 89–104.

- [49] P. Wang, W. Yao, A new weakly supervised approach for als point cloud semantic segmentation, *ISPRS Journal of Photogrammetry and Remote Sensing* 188 (2022) 237–254. doi:10.1016/j.isprsjprs.2022.04.016.
- [50] H. Yue, Q. Wang, M. Zhang, Y. Xue, L. Lu, 2d–3d fusion approach for improved point cloud segmentation, *Automation in Construction* 177 (2025) 106336. doi:10.1016/j.autcon.2025.106336.
- [51] D. Rozenberszki, O. Litany, A. Dai, Language-grounded indoor 3d semantic segmentation in the wild, in: *European Conference on Computer Vision*, Springer, 2022, pp. 125–141. doi:10.1007/978-3-031-19827-4\_8.
- [52] R. Pierdicca, M. Paolanti, F. Matrone, M. Martini, C. Morbidoni, E. S. Malinvern, E. Frontoni, A. M. Lingua, Point cloud semantic segmentation using a deep learning framework for cultural heritage, *Remote Sensing* 12 (6) (2020) 1005. doi:10.3390/rs12061005.
- [53] D. P. Kingma, J. Ba, Adam: A method for stochastic optimization (2017). arXiv:1412.6980, doi:10.48550/arXiv.1412.6980.  
URL <https://arxiv.org/abs/1412.6980>